

# JWST unveils heavily obscured (active and passive) sources up to $z \sim 13$

G. Rodighiero<sup>1,2\*</sup>, L. Bisigello<sup>1,2</sup>, E. Iani<sup>3</sup>, A. Marasco<sup>2</sup>, A. Grazian<sup>2</sup>, F. Sinigaglia<sup>1,2</sup>, P. Cassata<sup>1,2</sup> and C. Gruppioni<sup>4</sup>

<sup>1</sup>Dipartimento di Fisica e Astronomia, Università di Padova, Vicolo dell'Osservatorio, 3, I-35122, Padova, Italy

<sup>2</sup>INAF–Osservatorio Astronomico di Padova, Vicolo dell'Osservatorio 5, I-35122, Padova, Italy

<sup>3</sup>Kapteyn Astronomical Institute, University of Groningen, P.O. Box 800, 9700AV Groningen, The Netherlands

<sup>4</sup>INAF–Osservatorio di Astrofisica e Scienza dello Spazio di Bologna, Via Gobetti 93/3 - 40129 Bologna - Italy

Accepted XXX. Received YYY; in original form ZZZ

## ABSTRACT

A wealth of extragalactic populations completely missed at UV-optical wavelengths has been identified in the last decade, combining the deepest *HST* and *Spitzer* observations. These dark sources are thought to be very dusty and star-forming systems at  $3 < z < 5$ , and major contributors to the stellar mass build up. *JWST* is now promising to detect such objects well beyond the end of the Epoch of Reionization. In this Letter we report an investigation of the deep *JWST* survey in the SMACS0723 cluster, analysing NIRCам and MIRI images. We search for sources in the F444W band that are undetected in the F200W catalogues. We characterise the main properties of these sources via detailed SED modelling that account for a wide set of parameters and star formation histories, after a careful determination of their photometry. Among a robust sample of 20 candidates, we identify a mixed population of very red sources. We highlight the identification of candidate evolved systems, with stellar masses  $M_* \sim 10^{9-11} M_\odot$  at  $8 < z < 13$  characterized by unexpectedly important dust content at those epochs ( $A_V$  up to  $\sim 5.8$ mag), challenging current model predictions. We further identify an extremely red source (F200W-F440W  $\sim 7$ mag) that can be reproduced only by the spectrum of a passive, quenched galaxy of  $M_* \sim 10^{11.8} M_\odot$  at  $z \sim 5$ , filled of dust ( $A_V \sim 5$ mag).

**Key words:** galaxies: high-redshift – galaxies: evolution – infrared: galaxies

## 1 INTRODUCTION

The statistical identification of galaxies at various cosmic epochs is key to understand their formation and evolution. In the deepest extragalactic fields, multiwavelength observational efforts (from the X-ray to the radio spectral region) allowed for a reconstruction of the distinct galaxy populations and their formation history. The measurement of the star formation rate density (SFRD) is a key finding (e.g. Madau & Dickinson 2014). The SFRD peaked at  $z \sim 1-3$  and then descended quickly to the current period. However, recent studies have suggested that the portion of the SFRD hidden by dust and so unaccounted for by optical/UV surveys at  $z > 2$  is not negligible and is likely to increase with redshift at least up to  $z \sim 5-6$  (e.g. Novak et al. 2017, Gruppioni et al. 2020). Thus, a thorough investigation of high redshift galaxies is crucial for our comprehension of the early epochs of galaxy stellar mass growth.

The more traditional method of analyzing sources at  $z > 3$  relies on their broadband colors, as they allow to identify the presence of a brightness drop (i.e. the Lyman Break or the Lyman Forest). Such objects are known as Lyman-Break Galaxies (LBGs). Although this method is relatively simple to use, it is also significantly incomplete and contaminated. In particular, the LBG selection is known to be significantly biased towards relatively young massive and starforming galaxies ( $M_* \gtrsim 10^{11} M_\odot$ ; van Dokkum et al. 2006; Bian et al. 2013).

Other independent near-IR color schemes have thus been suggested to extend the census of the high- $z$  population, in particular thanks to the *Spitzer* space telescope. Wang et al. (2016) provide a strategy that allows for a rather clear selection of  $z > 3$  galaxies. In particular, the color cut  $H - [4.5] > 2.25$  is proposed to select old or dusty galaxies at  $z > 3$  (called HIEROs) that are completely missed even by the deepest *Hubble* Space Telescope (*HST*) imaging. Such UV-optically dark objects are dominated by obscured and dusty systems, including submillimeter sources (Wang et al. 2019). HIEROs have typical  $M_* \gtrsim 10^{10} M_\odot$  and  $\text{SFR} \gtrsim 20 M_\odot/\text{yr}$  at an average  $z \sim 4$ . They exhibit low number space densities and active star formation, contributing up to  $\sim 20\%$  of the SFRD at  $z \sim 3$  to 5 (e.g. Gruppioni et al. 2020; Sun et al. 2021; Talia et al. 2021; Enia et al. 2022), and up to 50% of the bright end of the stellar mass function (Rodighiero et al. 2007). Despite the significance of these galaxies, most of their physical characteristics are still very speculative, with the exception of a few spectroscopic confirmations (Wang et al. 2019; Caputi et al. 2021). The James Webb Space Telescope (*JWST*) has just opened a new window on the distant Universe, allowing through its near-to-mid IR eyes to detect farther and fainter sources. In this Letter we exploit the first deep field imaging offered by the early release observations (ERO) to demonstrate the ability of *JWST* to identify HIEROs like sources missed even by *Spitzer* because of their fainter luminosities. By combining the Near-Infrared Camera (NIRCам; Rieke et al. 2005) and Mid Infrared Instrument (MIRI; Rieke et al. 2015) photometry, we investigate the properties of the most robust

\* E-mail: mn@ras.org.uk (KTS)

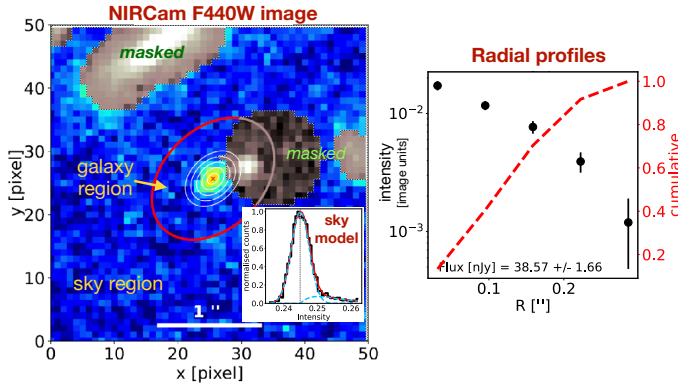


**Figure 1.** Example of our photometric analysis on the NIRCам F444W image of target #15. *Left panel:* image cutout. A red ellipse marks the division between galaxy and sky regions. The white ellipses show the rings used to extract radial profiles. Masked regions are shown with grey shades. The inset shows our sky model made by a combination of a Gaussian and a Schechter component (see text). *Right panel:* radial intensity profile, in image units (points with error-bars), and normalised growth curve (red dashed curve).

detections, highlighting: i) the discovery of extremely dusty low mass systems, filling the faint end of the HIEROs mass function; ii) the potential identification of massive quenched galaxies at  $z \sim 5$ ; iii) the confirmation of high- $z$  systems ( $8 < z < 13$ ) as already probed by *JWST* (Adams et al. 2022; Atek 2022; Carnall et al. 2022a; Castellano et al. 2022; Donnan et al. 2022; Finkelstein et al. 2022; Naidu et al. 2022), but with large dust content. Throughout the paper, we consider a  $\Lambda$ CDM cosmology with  $H_0 = 70 \text{ km s}^{-1} \text{ Mpc}^{-1}$ ,  $\Omega_M = 0.27$ ,  $\Omega_\Lambda = 0.73$  and a Kroupa (2001) stellar Initial Mass Function; all magnitudes are in the AB system.

## 2 JWST OBSERVATIONS OF SMACS0723

The Reionization Lensing Cluster Survey (RELICS, Coe et al. 2019) dedicated 188 HST orbits and 946 Spitzer hours, observing 41 of the most massive galaxy clusters discovered by Planck at redshift  $z \sim 0.2 - 1.0$ . The relatively deep ACS and WFC3/IR imaging, spanning  $0.4 - 1.7 \mu\text{m}$ , has been used to derive accurate magnification maps of these clusters. The cluster SMACS J0723.3–7327 (hereafter SMACS0723) at  $z = 0.39$  has two lens models (Glafic and Lenstool), publicly available in the RELICS repository<sup>1</sup>. According to these maps, the magnification region at  $\mu \geq 100$  is relatively extended, allowing the selection of galaxies at  $z \sim 6 - 8$  (Salmon et al. 2020).

The observations of SMACS0723 by the world’s premier space science observatory *JWST* marked the official beginning of the highly promising observatory’s science operations (Pontoppidan et al. 2022). The high quality of the Webb first images and spectra of SMACS0723 have been obtained in particular with the instruments NIRCам and MIRI. The ERO program aims at demonstrating the ability of *JWST* to image high-redshift galaxies, at a depth unrivaled by HST or ground based telescopes.

### 2.1 NIRCам images

The NIRCам instrument targeted SMACS0723, pointing one detector on the cluster, and the other detector on the adjacent off-field. The NIRCам filters F090W, F150W, F200W, F277W, F356W, and F444W have been exposed for  $\sim 7500$  seconds each, resulting in a  $5\sigma$  sensitivity limit of  $\sim 28.5 - 29.6$  AB magnitude for point-like sources. These depths are equivalent to the ones obtained with WFC3/IR for the HUDF12 pointing (Koekemoer et al. 2013), and they are a factor of 10 times more sensitive than the deepest *Spitzer*/IRAC imaging available at  $3.6$  and  $4.5 \mu\text{m}$ .

The NIRCам reduced images have been retrieved from the Mikulski Archive for Space Telescopes (MAST)<sup>2</sup>. The official reduction has overall good quality, with slightly off-centering problems of alignment between the different bands. In order to overcome this issue, we decided to carry out a first catalog in each band using SExtractor (Bertin & Arnouts 1996), matching a posteriori the catalogs in absolute coordinates. The matched catalog has been used in order to pre-select high- $z$  galaxy candidates with the dropout technique. As described in Section 2.3, a detailed photometric analysis has been applied on the relevant sources only.

### 2.2 MIRI images

The MIRI instrument observed the central region of SMACS0723 with the F770W, F1000W, F1500W and F1800W filters. The MIRI observations cover only part of the NIRCам field, given the difference in the field-of-view of the two instruments (i.e.  $112.6'' \times 73.5''$  for MIRI, two  $2.2' \times 2.2'$  for NIRCам).

Differently from NIRCам, the MIRI fully reduced images available on MAST show the presence of strong background patterns (e.g. vertical striping and gradients). The prominence of these features varies significantly among filters. Since such a background could impact on the number of detections and photometric quality of our sample, we decide to re-run the *JWST* pipeline<sup>3</sup> (v. 1.6.1) adding an additional step to improve the background cleaning and homogenization. The final result is not purely cosmetic: a SExtractor run on the final image shows that we are able to minimize spurious detections while maximizing the number of real sources. Besides, the magnitude of bright sources is not affected. This ensures us that the extra-cleaning of the background does not impact on our magnitude estimates. As for NIRCам, we use SExtractor to correct the astrometry of the MIRI images.

### 2.3 Sample selection

We propose to identify potential high- $z$  and/or dusty sources by selecting F200W dropouts candidates in the SMACS0723 *JWST* deep field. Indeed, these objects could be interpreted either as: i)  $z > 10$  LBGs, ii) heavily extinguished galaxies iii) red and dead passive sources at  $3 < z < 6$ . We start from the SExtractor photometry in the different NIRCам bands (see Sect. 2.1), we cross-match the single bands extractions to the F444W catalog adopting a  $0.2$  arcsec search radius. We look for sources with a F444W  $\text{mag} < 29 \text{ mag [AB]}$  detection (above the  $5\sigma$  depth) and we select a sample of F200W dropouts that lack a counterpart in the F200W band. We visually inspected each candidate, removing all spurious or contaminated objects. We

<sup>1</sup> <https://archive.stsci.edu/missions/hlsp/relics/smacs0723-73/models/>

<sup>2</sup> <https://archive.stsci.edu>

<sup>3</sup> <https://jwst-pipeline.readthedocs.io/en/latest/index.html>

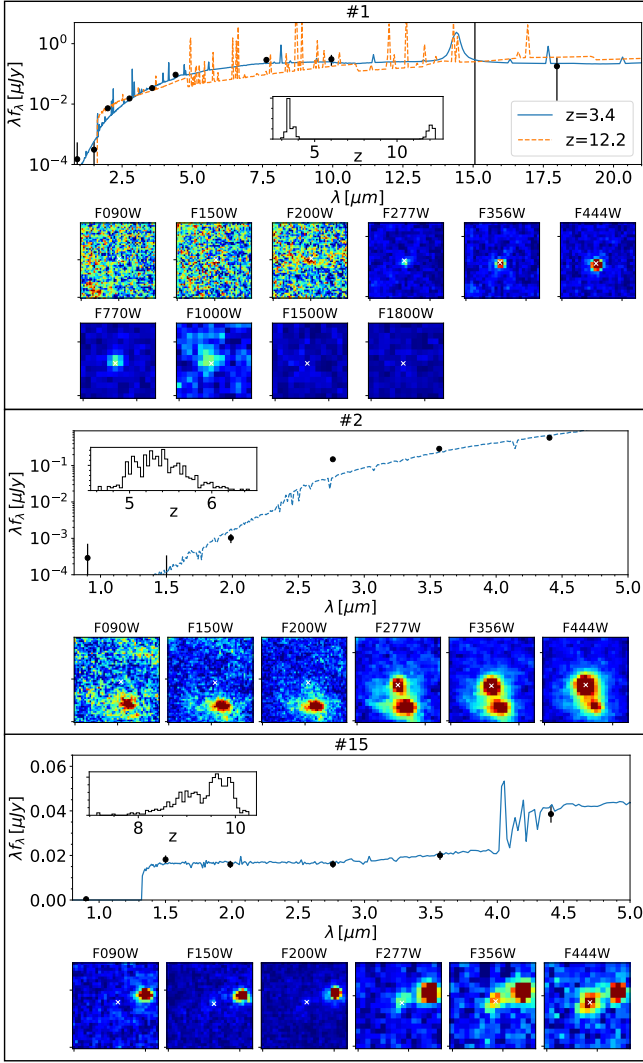


**Figure 2.** Photometry and best fit model of the galaxies #1 (top), #2 (middle) and #15 (bottom). The inset show the probability redshift distribution. We also report cut out images of the NIRCам/MIRI filters for the same galaxies, whose position is shown with a white cross.

identify a robust sample of 20 sources, for which we perform a refined photometric measurement (see Section 2.4), in order to avoid biases due to local background variations in the NIRCам and MIRI maps. The coordinates and multiwavelength fluxes of the final sample are presented in table 1. We note that some non-detections at wavelengths shorter than F200W in the preliminary SExtractor catalogs are instead very faint detections after our detailed photometric analysis. The nature of the sources will be investigated through SED fitting in Section 4.

#### 2.4 Ad hoc source photometry

Our photometric analysis is based on the extraction of cumulative light profiles from sky-subtracted images after the removal of contamination from point-like and extended sources. We provide a brief description of our method below, using the NIRCам F444W image of target #15 as a working example (Fig. 1), but the same approach

is used for all the other JWST images. More detailed information on the method will be provided by Marasco et al. (*in prep.*).

We first extract cutouts of  $50 \times 50$  pixels, centered at the coordinates of the target. Each cutout is visually inspected for the presence of strong contaminants (such as an off-centered bright galaxy, or the diffraction figure from a nearby source), which are manually masked and excluded from the analysis. The image is then partitioned in two regions: a ‘sky’ region, where the contribution of the target is negligible, and a ‘galaxy’ region, where the target flux is dominant. This partition is based on an ellipse (shown in red in the left panel of Fig. 1), whose axial ratio and orientation are manually adjusted after visual inspection. To determine the image background  $b$  and noise  $\sigma$ , we model the pixel intensity distribution in the sky region using a two component model made by the sum of a Gaussian and a Schechter function (inset in Fig. 1). The latter accounts for possible contamination within the galaxy region. We take the mean and the standard deviation of the former as fiducial values for  $b$  and  $\sigma$ , respectively. The background is subtracted from the cutout before the next analysis steps.

The galaxy region is partitioned into a series of rings, with inter-ring separation of one pixel. A radial profile is extracted by computing the mean intensity of all the non-masked pixels in each ring, and is used to derive the cumulative profile (or ‘growth curve’), for which masked pixels in a given ring are replaced with the mean intensity computed in that ring (right panel in Fig. 1). Profiles are truncated where the signal-to-noise ratio (SNr) in a given ring drops below unity: this corresponds to measuring fluxes using a *variable* aperture, with a size that is tuned to the properties of each target. Targets with sufficiently good SNr feature a visible flattening in their growth curve, which is a key check for the goodness of their photometry. Finally, MIRI fluxes are corrected for aperture effects, using simulated MIRI point spread functions<sup>4</sup>. This step is not necessary for NIRCам images, where the adopted apertures are large enough to enclose virtually all of the PSF light.

Flux uncertainties are determined with a Monte-Carlo technique: we re-compute  $N$  times the flux by injecting Gaussian noise into the image, and take the standard deviation of the resulting flux distribution as our fiducial uncertainty.

### 3 SED FITTING

We derived the redshift and galaxy physical properties (e.g. stellar mass, SFR) using the Bayesian Analysis of Galaxies for Physical Inference and Parameter ESTimation (BAGPIPES; Carnall et al. 2018). In particular, we consider Bruzual & Charlot (2003) stellar population models with stellar metallicity from 0.005 solar up to solar. We allow the code to explore the redshift range  $0 < z < 15$  and the stellar mass range up to  $10^{12.5} M_{\odot}$ . Nebular emission lines were included assuming a ionization parameter of  $10^{-3}$  and we considered the same reddening law (i.e., Calzetti et al. 2000) for both the stellar continuum and the nebular emission lines. We run the code twice, once with an exponentially declining (i.e.  $\text{SFR} \propto e^{-(t/\tau)}$ ) star-formation history and once with a rising (i.e.  $\text{SFR} \propto t e^{-(t/\tau)}$ ) one, both with ages ranging from 1 Myr to the age of the Universe and  $\tau = 0.01$  to 10 Gyr. Between these two runs, we kept the fit with the minimum  $\chi^2$ , but we highlight that redshift, stellar mass and SFR are, for the majority of cases, consistent between the two cases. We show the fits of source #1, #2 and #15 as examples in Figure 2.

<sup>4</sup> <https://jwst-docs.stsci.edu/jwst-mid-infrared-instrument/miri-performance/miri-point-spread-functions>

ID	RA h m s	DEC d m s	$f_{F090W}$ nJy	$f_{F150W}$ nJy	$f_{F200W}$ nJy	$f_{F277W}$ nJy	$f_{F356W}$ nJy	$f_{F444W}$ nJy	$f_{F770W}$ nJy	$f_{F1000W}$ nJy	$f_{F1500W}$ nJy	$f_{F1800W}$ nJy
1	7:23:16.79	-73:26:41.72	0.15±0.39	0.31±0.27	7.24±0.74	15.31±1.53	33.84±3.38	93.67±9.37	353.59±77.16	393.37±155.32	0.0±36.66	178.68±165.84
2	7:22:50.39	-73:28:17.63	0.29±0.42	0.01±0.33	1.03±0.29	148.9±14.89	289.31±28.93	581.58±58.16	—	—	—	—

(abridged)

**Table 1.** Position and photometry in the available NIRCcam and MIRI filters of the 20 F200W dropouts. We applied aperture correction to the MIRI photometry, when necessary. The complete table is available online.

ID	z	$\log_{10}(M/M_{\odot})$	$\log_{10}(\text{SFR}/M_{\odot}\text{yr}^{-1})$	$A_V$	$\chi^2_{1,gal}$	z	$\log_{10}(M/M_{\odot})$	$\log_{10}(\text{SFR}/M_{\odot}\text{yr}^{-1})$	$A_V$	$\chi^2_{1,gal}$	$\chi^2_{red,BD}$	$\mu$
1 <sup>st</sup> solution												
1	12.1 <sup>+0.1</sup> <sub>-0.2</sub>	9.6 <sup>+0.1</sup> <sub>-0.1</sub>	1.65 <sup>+0.08</sup> <sub>-0.1</sub>	2.5 <sup>+0.2</sup> <sub>-0.1</sub>	7.02	3.4 <sup>+0.2</sup> <sub>-0.1</sub>	9.4 <sup>+0.2</sup> <sub>-0.1</sub>	0.67 <sup>+0.12</sup> <sub>-0.20</sub>	4.1 <sup>+0.3</sup> <sub>-0.4</sub>	23.86	2527.55	2.65±0.35
2	5.3 <sup>+0.4</sup> <sub>-0.2</sub>	11.8 <sup>+0.1</sup> <sub>-0.1</sub>	-0.38 <sup>+0.81</sup> <sub>-0.1</sub>	5.2 <sup>+0.3</sup> <sub>-0.3</sub>	58.08	—	—	—	—	—	23227.74	—
3	6.2 <sup>+0.5</sup> <sub>-0.7</sub>	10.7 <sup>+0.3</sup> <sub>-0.3</sub>	2.35 <sup>+1.25</sup> <sub>-0.28</sub>	3.6 <sup>+0.2</sup> <sub>-0.3</sub>	3.60	2.6 <sup>+0.3</sup> <sub>-0.1</sub>	9.7 <sup>+0.2</sup> <sub>-0.3</sub>	1.06 <sup>+0.19</sup> <sub>-0.19</sub>	5.7 <sup>+0.2</sup> <sub>-0.3</sub>	9.44	4919.05	—
4	6.0 <sup>+0.3</sup> <sub>-0.3</sub>	10.4 <sup>+0.1</sup> <sub>-0.1</sub>	1.00 <sup>+0.42</sup> <sub>-0.19</sub>	1.8 <sup>+0.5</sup> <sub>-0.4</sub>	31.16	—	—	—	—	—	5256.14	1.5±0.1
5	5.9 <sup>+0.3</sup> <sub>-0.3</sub>	8.8 <sup>+0.2</sup> <sub>-0.1</sub>	0.57 <sup>+0.14</sup> <sub>-0.14</sub>	1.5 <sup>+0.2</sup> <sub>-0.2</sub>	4.65	—	—	—	—	—	100.59	—
6	1.8 <sup>+1.2</sup> <sub>-0.3</sub>	8.1 <sup>+0.2</sup> <sub>-0.2</sub>	-0.75 <sup>+0.62</sup> <sub>-0.18</sub>	1.3 <sup>+0.3</sup> <sub>-0.3</sub>	1.98	0.5 <sup>+0.1</sup> <sub>-0.1</sub>	7.3 <sup>+0.2</sup> <sub>-0.2</sub>	-2.25 <sup>+0.23</sup> <sub>-0.43</sub>	3.6 <sup>+0.5</sup> <sub>-0.5</sub>	2.61	196.99	—
7	0.1 <sup>+0.1</sup> <sub>-0.0</sub>	6.2 <sup>+0.6</sup> <sub>-0.5</sub>	-3.68 <sup>+0.17</sup> <sub>-0.55</sub>	2.9 <sup>+0.6</sup> <sub>-0.7</sub>	1.38	—	—	—	—	—	41.14	—
8	0.2 <sup>+0.0</sup> <sub>-0.0</sub>	5.2 <sup>+0.2</sup> <sub>-0.2</sub>	-2.79 <sup>+0.12</sup> <sub>-0.18</sub>	0.9 <sup>+0.3</sup> <sub>-0.3</sub>	14.28	—	—	—	—	—	20.32	—
9	0.4 <sup>+0.1</sup> <sub>-0.1</sub>	7.2 <sup>+0.2</sup> <sub>-0.3</sub>	-3.03 <sup>+0.63</sup> <sub>-0.3</sub>	6.0 <sup>+0.9</sup> <sub>-0.6</sub>	33.66	—	—	—	—	—	261.18	—
10	5.2 <sup>+0.1</sup> <sub>-0.1</sub>	8.6 <sup>+0.1</sup> <sub>-0.1</sub>	-0.15 <sup>+0.11</sup> <sub>-0.12</sub>	0.6 <sup>+0.2</sup> <sub>-0.1</sub>	1.45	—	—	—	—	—	233.22	—
11	1.5 <sup>+0.6</sup> <sub>-0.2</sub>	7.6 <sup>+0.2</sup> <sub>-0.2</sub>	-1.42 <sup>+0.35</sup> <sub>-0.33</sub>	0.8 <sup>+0.7</sup> <sub>-0.4</sub>	2.01	0.5 <sup>+0.1</sup> <sub>-0.1</sub>	6.6 <sup>+0.2</sup> <sub>-0.2</sub>	-2.43 <sup>+0.28</sup> <sub>-0.25</sub>	2.4 <sup>+0.4</sup> <sub>-0.4</sub>	5.74	81.25	—
12	5.2 <sup>+0.1</sup> <sub>-0.1</sub>	7.7 <sup>+0.1</sup> <sub>-0.2</sub>	-0.29 <sup>+0.36</sup> <sub>-0.16</sub>	1.2 <sup>+0.1</sup> <sub>-0.1</sub>	4.98	3.5 <sup>+0.1</sup> <sub>-0.1</sub>	7.9 <sup>+0.1</sup> <sub>-0.1</sub>	-0.08 <sup>+0.10</sup> <sub>-0.10</sub>	1.4 <sup>+0.1</sup> <sub>-0.2</sub>	11.41	393.85	1.5±0.1
13	1.5 <sup>+0.1</sup> <sub>-0.1</sub>	7.0 <sup>+0.1</sup> <sub>-0.1</sub>	-1.01 <sup>+0.03</sup> <sub>-0.04</sub>	3.7 <sup>+0.2</sup> <sub>-0.2</sub>	53.73	5.6 <sup>+0.4</sup> <sub>-0.5</sub>	9.0 <sup>+0.1</sup> <sub>-0.1</sub>	-0.15 <sup>+0.35</sup> <sub>-0.3</sub>	0.9 <sup>+0.4</sup> <sub>-0.6</sub>	80.72	274.24	1.7±0.2
14	10.2 <sup>+0.6</sup> <sub>-0.4</sub>	11.8 <sup>+0.2</sup> <sub>-0.2</sub>	3.35 <sup>+0.11</sup> <sub>-0.48</sub>	5.8 <sup>+0.1</sup> <sub>-0.3</sub>	0.46	11.5 <sup>+0.3</sup> <sub>-0.9</sub>	11.1 <sup>+0.5</sup> <sub>-0.3</sub>	3.06 <sup>+0.46</sup> <sub>-0.25</sub>	5.8 <sup>+0.1</sup> <sub>-0.5</sub>	1.24	65.64	—
15	9.5 <sup>+0.4</sup> <sub>-0.6</sub>	8.9 <sup>+0.1</sup> <sub>-0.2</sub>	0.46 <sup>+0.16</sup> <sub>-0.17</sub>	0.4 <sup>+0.1</sup> <sub>-0.1</sub>	3.01	—	—	—	—	—	117.88	—
16	4.5 <sup>+0.6</sup> <sub>-0.3</sub>	8.8 <sup>+0.2</sup> <sub>-0.2</sub>	0.51 <sup>+0.17</sup> <sub>-0.19</sub>	1.5 <sup>+0.3</sup> <sub>-0.2</sub>	24.95	—	—	—	—	—	239.99	12.3±3.9
17	0.4 <sup>+0.1</sup> <sub>-0.1</sub>	6.1 <sup>+0.4</sup> <sub>-0.3</sub>	-2.21 <sup>+0.24</sup> <sub>-0.24</sub>	4.0 <sup>+1.0</sup> <sub>-0.9</sub>	0.14	5.2 <sup>+0.4</sup> <sub>-0.4</sub>	8.3 <sup>+0.4</sup> <sub>-0.4</sub>	0.23 <sup>+0.29</sup> <sub>-0.26</sub>	1.7 <sup>+0.9</sup> <sub>-0.4</sub>	0.33	36.16	—
18	6.7 <sup>+0.1</sup> <sub>-0.6</sub>	10.8 <sup>+0.2</sup> <sub>-0.3</sub>	2.34 <sup>+0.37</sup> <sub>-0.3</sub>	3.9 <sup>+0.6</sup> <sub>-0.4</sub>	5.24	5.0 <sup>+0.8</sup> <sub>-0.2</sub>	10.6 <sup>+0.1</sup> <sub>-0.1</sub>	1.86 <sup>+0.25</sup> <sub>-0.18</sub>	4.0 <sup>+0.4</sup> <sub>-0.4</sub>	6.51	8703.25	—
19	8.3 <sup>+2.6</sup> <sub>-0.5</sub>	10.3 <sup>+0.7</sup> <sub>-0.6</sub>	1.92 <sup>+0.86</sup> <sub>-0.62</sub>	4.8 <sup>+0.4</sup> <sub>-1.0</sub>	4.91	—	—	—	—	—	14.77	39.5±33.6
20	5.3 <sup>+0.5</sup> <sub>-0.2</sub>	8.4 <sup>+0.1</sup> <sub>-0.2</sub>	-0.05 <sup>+0.12</sup> <sub>-0.15</sub>	0.8 <sup>+0.2</sup> <sub>-0.1</sub>	8.97	—	—	—	—	—	133.60	—

**Table 2.** Results from the SED fitting analysis. Columns 2 to 6 show the redshift, stellar mass, SFR,  $A_V$  and  $\chi^2$  of the best solution derived with BAGPIPES, while we report in columns 7 to 11 the same quantities for the secondary solution, when present. In column 12 we report the  $\chi^2$  obtained using templates of brown dwarfs. The magnification due to gravitational lensing, derived averaging the magnification of the Glafic and Lenstool models, at the redshift of the first solution is listed in column 13. The magnification is not reported for galaxies outside the cluster, i.e. in the adjacent off-field, or in foreground (#8 and #9).

The spectral properties of a local brown dwarf can resemble the rest-frame optical observations of high- $z$  galaxies. Therefore, we also fit our candidates dropouts with L and T dwarf models available from Burrows et al. (2006). Such templates span effective temperatures between 700 K and 2300 K, metallicities between  $[\text{Fe}/\text{H}]=-0.5$  and 0.5 and gravities between  $10^{4.5}$  and  $10^{5.5} \text{ cm s}^{-2}$ .

We performed the SED fitting allowing the extinction parameter to span the range of values  $0 < A_V < 6$ . Values of  $A_V$  exceeding  $\sim 6$  mag have been observed only in the the central 1–2 kpc of local luminous IR galaxies (Mayya et al. 2004; Scoville et al. 2015). In comparison, dusty submillimeter galaxies at  $2 < z < 3$  have typical average extinction around  $A_V \sim 2.5$  (Knudsen et al. 2005; da Cunha et al. 2015). Another class including heavily obscured sources is that of dusty extremely red objects. However, even in this case the reddening has typical values around  $A_V < 4.0$  at  $3 < z < 6$  (Wang et al. 2019; Barrufet et al. 2022). Results from this SED fitting analysis are reported in Table 2.

## 4 RESULTS

### 4.1 Nature of the F444W sources without a F200W counterpart

We rely on the SED fitting approach described in Section 3 to infer the physical properties of our sample. A summary of the photometric redshifts and basic outputs from BAGPIPES is reported in Table 2. When the posterior distribution of the physical parameters derived with BAGPIPES show two or more separate peaks, we report the two most probable solutions. Fig. 3 summarizes the position of the sources in the  $M_*$ -SFR plane at their best assigned photo- $z$  (corrected

for magnification when required). The sources can be grouped in the following main classes.

#### Low redshift contaminants ( $z < 2$ )

- **Red and dusty low- $z$  dwarf galaxies:** the SED of four sources are reproduced with templates of  $z < 0.5$  galaxies, low stellar masses  $\log(M_*/M_{\odot}) \sim 5-7$ , and SFR consistent with the faint end of the Main Sequence (MS) in the local Universe (Fig. 3 top-left). These sources are less massive even than Low Surface Brightness (LSB) galaxies at  $z = 0$  (e.g. McGaugh et al. 2017). However, the *JWST* dwarves are much more extinguished than traditional UV selection, with  $A_V$  up to  $\sim 6$  mag (IDs #7, 8, 9, 17).

- **Low-mass star forming sources at Cosmic Noon:** the selection also includes normal MS galaxies at  $z \sim 1.5 - 1.8$ , with  $\log(M_*/M_{\odot}) \sim 7-8$ , probing the faint end of the Main Sequence (e.g. Bisigello et al. 2018; Rodríguez-Muñoz et al. 2022, IDs #6, 11, 13, Fig. 3 top-right).

Having recognized the lower redshift contaminants, we are then left with higher- $z$  candidates, most of them being unreachable or unidentifiable before the *JWST*.

#### Distant sources ( $4 < z < 13$ )

- **$4 < z < 6$  dusty star-forming systems:** 40% of the sample sits on the MS at  $z \sim 4 - 6$ , part of them filling the obscured faint end of the Main Sequence missed by LBGs (similar to Barrufet et al. (2022), IDs #3, 4, 5, 10, 12, 16, 18, 20, Fig. 3 bottom-left). In particular, #3, 4 and 18 also satisfy the HIERO definition  $F200W-F440W > 2.3$  mag, due to their larger extinction parameter ( $A_V \sim 3$ ). As discussed in Section 1, this population was completely missed by *HST* and *Spitzer*, lacking the sensitivity to statistically identify  $[4.5] > 24$  mag optically



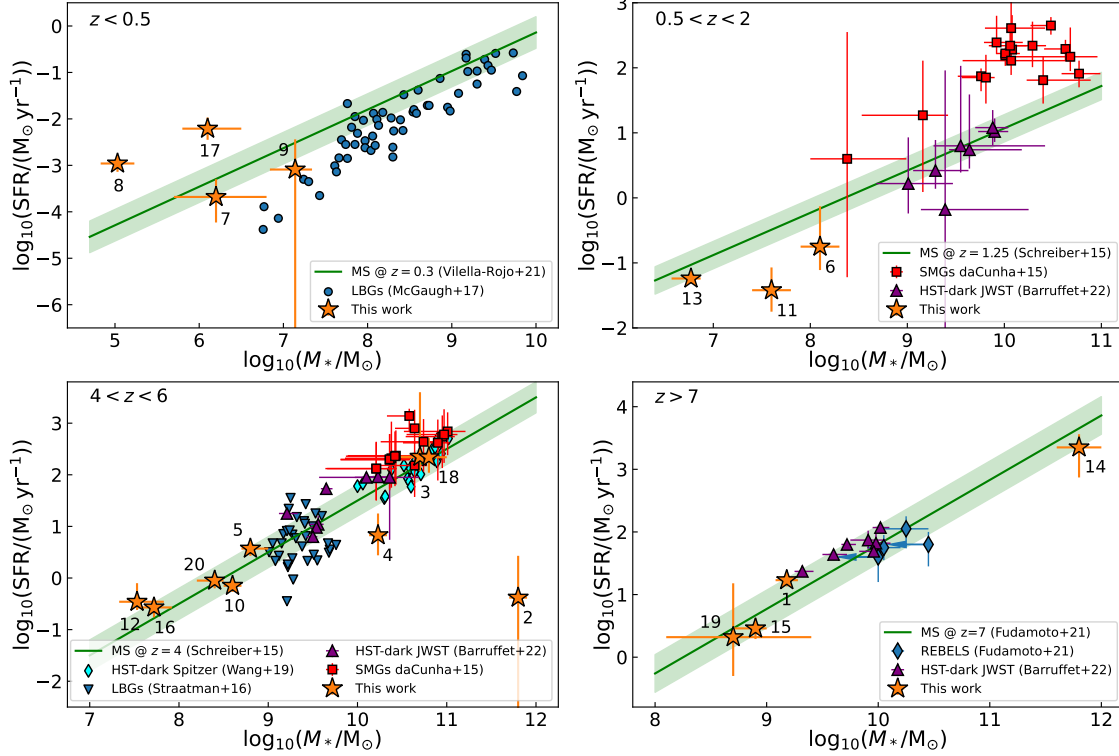


**Figure 3.** SFR vs stellar mass distribution of the sources presented in Table 2. The four panels compare our sample with the most relevant populations at the corresponding redshift interval. References to the various data-sets are reported in the inset of each panel. Objects in our sample (filled orange stars) are marked with their ID as in Table 2. Lensed sources have been de-magnified in this Figure.

dark sources, but they could play a major role in the stellar assembly of today’s massive galaxies.

• **A quenched, dusty and massive galaxy at  $z \sim 5$ ?** We identify the most extreme red object in our sample (F200W-F440W  $\sim 7$  mag), that can be explained only by templates of a massive ( $\log(M_*/M_\odot) \sim 11.8$ ) quenched galaxy at  $z \sim 5$  with anomalous abundant dust extinction,  $A_V = 5.5$  mag (ID #2). This object is even redder than the JWST source with SCUBA2 analysed by (Zavala et al. 2022), which is at a similar redshift but it is starbursting. We verify the presence of a possible less dusty solution by running BAGPIPES limiting the reddening to  $A_V < 2$ . However, the best solution results in a  $\chi^2$  that is three times larger than the solution with  $A_V = 5.2$ . We also varied the ionization parameter (U) to test if the red colors of this galaxy could be due to the presence of nebular emission lines. However, even with  $\log(U) = -2$  and  $-4$ , the best solution remains a galaxies a galaxy around  $z = 5$  and with  $A_V \sim 5$ . While passive sources at  $3 < z < 5$  are already emerging in JWST early observations (Carnall et al. 2022b), the existence of a dusty, massive and quenched source at  $z = 5$  could represent the precursor of dust rich quiescent galaxies at  $z \sim 2$  (Gobat et al. 2018).

• **Extinguished high- $z$  star-forming sources ( $8 < z < 13$ ):** the daily recording of the farthest objects with JWST is currently providing candidates up to  $z \sim 17$  (e.g. Harikane et al. 2022). These sources are consistent with primordial young star forming galaxies, with a negligible dust content. Indeed, the common LBG technique used to select them privileges UV blue and bright spectral types. In our approach we include redder populations, and we do not limit the extinction parameter while fitting the observed SEDs. Surprisingly, we classify four objects (ID #1, 14, 15, 19) at  $z > 8$ , with mature stellar populations ( $\log(M_*/M_\odot) \sim 9-11$ ) that differ from already detected

JWST sources at similar cosmic epochs for their extreme dust content ( $A_V = 0.4 - 5.8$  mag). Fudamoto et al. (2021) report the ALMA C II detection of two sources at  $z \sim 6 - 7$ , providing additional evidence for the existence of obscured systems that could contribute on the order of  $\sim 20\%$  to the  $z > 6$  cosmic SFRD. Such objects are currently unexplained by theoretical models. Ferrara et al. (2022) provide a possible explanation based on the assumption that dust has been efficiently ejected during the early stages of galaxy formation. Our results bring the attention to a potentially unexplored evolution of dust production and dust lifetime in the primeval Universe. In particular, we highlight source #1, the only object securely detected even in two MIRI bands (F770W and F1000W). The NIRCAM+MIRI photometry provides stronger constraints on the SED fitting, turning a primary solution at  $z = 12.1$  (see Fig 2, with the source sitting on the extrapolated MS at  $z > 8$  (see Fig. 3 bottom-right). Compared to the other UV bright sources at the same cosmic epoch, #1 has an extinction best-fit of  $A_V = 2.5$  mag. A secondary dusty solution at  $z = 3.4$  is disadvantaged by the  $\chi^2$ .

By selecting and photometrically characterizing NIRCAM F444W sources in the SMACS0723 deep field that lack a F200W counterpart, we provide only a first glimpse on the potential of the JWST to uncover new galaxy populations. We remind that their classification remains still speculative, until upcoming spectroscopic follow-ups will systematically constrain their distance and nature.

**DATA AVAILABILITY:** The data underlying this article will be shared on reasonable request to the corresponding author.

## REFERENCES

- Adams N. J., et al., 2022, arXiv e-prints, p. [arXiv:2207.11217](#)
- Atek H. e. a., 2022, arXiv e-prints, p. [arXiv:2207.12338](#)
- Barrufet L., et al., 2022, arXiv e-prints, p. [arXiv:2207.14733](#)
- Bertin E., Arnouts S., 1996, *A&AS*, **117**, 393
- Bian F., et al., 2013, *ApJ*, **774**, 28
- Bisigello L., Caputi K. I., Grogan N., Koekemoer A., 2018, *A&A*, **609**, A82
- Bruzual G., Charlot S., 2003, *MNRAS*, **344**, 1000
- Burrows A., Sudarsky D., Hubeny I., 2006, *ApJ*, **640**, 1063
- Calzetti D., Armus L., Bohlin R. C., Kinney A. L., Koornneef J., Storchi-Bergmann T., 2000, *ApJ*, **533**, 682
- Caputi K. I., et al., 2021, *The Astrophysical Journal*, **908**, 146
- Carnall A. C., McLure R. J., Dunlop J. S., Davé R., 2018, *MNRAS*, **480**, 4379
- Carnall A. C., et al., 2022a, arXiv e-prints, p. [arXiv:2207.08778](#)
- Carnall A. C., et al., 2022b, arXiv e-prints, p. [arXiv:2208.00986](#)
- Castellano M., et al., 2022, arXiv e-prints, p. [arXiv:2207.09436](#)
- Coe D., et al., 2019, *ApJ*, **884**, 85
- Donnan C. T., et al., 2022, arXiv e-prints, p. [arXiv:2207.12356](#)
- Enia A., et al., 2022, *ApJ*, **927**, 204
- Ferrara A., Pallottini A., Dayal P., 2022, arXiv e-prints, p. [arXiv:2208.00720](#)
- Finkelstein S. L., et al., 2022, arXiv e-prints, p. [arXiv:2207.12474](#)
- Fudamoto Y., et al., 2021, *Nature*, **597**, 489
- Gobat R., et al., 2018, *Nature Astronomy*, **2**, 239
- Gruppioni C., et al., 2020, *Astronomy & Astrophysics*, **643**, A8
- Harikane Y., et al., 2022, arXiv e-prints, p. [arXiv:2208.01612](#)
- Knudsen K. K., et al., 2005, *ApJ*, **632**, L9
- Koekemoer A. M., et al., 2013, *ApJS*, **209**, 3
- Kroupa P., 2001, *MNRAS*, **322**, 231
- Madau P., Dickinson M., 2014, *ARAA*, **52**, 415
- Mayya Y. D., Bressan A., Rodríguez M. e. a., 2004, *ApJ*, **600**, 188
- McGaugh S. S., Schombert J. M., Lelli F., 2017, *ApJ*, **851**, 22
- Naidu R. P., et al., 2022, arXiv e-prints, p. [arXiv:2207.09434](#)
- Novak M., et al., 2017, *Astronomy & Astrophysics*, **602**, A5
- Pontoppidan K., et al., 2022, arXiv e-prints, p. [arXiv:2207.13067](#)
- Rieke M. J., Kelly D., Horner S., 2005, *SPIE*, **5904**
- Rieke G. H., et al., 2015, *PASP*, **127**, 584
- Rodighiero G., Cimatti A., Franceschini A. e. a., 2007, *A&A*, **470**, 21
- Rodríguez-Muñoz L., et al., 2022, *MNRAS*, **510**, 2061
- Salmon B., et al., 2020, *ApJ*, **889**, 189
- Scoville N., et al., 2015, *ApJ*, **800**, 70
- Sun F., et al., 2021, *ApJ*, **922**, 114
- Talia M., Cimatti A., Giuliotti M. e. a., 2021, *ApJ*, **909**, 23
- Wang T., et al., 2016, *ApJ*, **816**, 84
- Wang T., et al., 2019
- Zavala J. A., et al., 2022, arXiv e-prints, p. [arXiv:2208.01816](#)
- da Cunha E., et al., 2015, *ApJ*, **806**, 110
- van Dokkum P. G., et al., 2006, *ApJ*, **638**, L59

This paper has been typeset from a  $\text{\LaTeX}$  file prepared by the author.